

Extraction of Separation and Attachment Surfaces from Three-Dimensional Steady Shear Flows

A. Surana*

Massachusetts Institute of Technology, Cambridge, Massachusetts 02139

G. B. Jacobs†

San Diego State University, San Diego, California 92182

and

G. Haller‡

Massachusetts Institute of Technology, Cambridge, Massachusetts 02139

DOI: 10.2514/1.21464

We apply a recent analytic theory of three-dimensional steady separation to direct numerical simulations of backward-facing-step and lid-driven-cavity flows. We determine the exact location and slope of separation and attachment surfaces that have only been approximated heuristically in earlier studies. We also visualize the corresponding global separation and attachment surfaces, which reveal highly complex separated flow geometry.

Nomenclature

C	=	speed of sound
\mathbf{D}	=	rate of the strain tensor
e	=	internal energy
\mathbf{g}	=	separation curve slope
h	=	inflow channel height
\mathbf{I}	=	identity matrix
L	=	length
\mathcal{L}	=	separation curve
Ma	=	Mach number
M_f	=	reference Mach number
Pr	=	Prandtl number
p	=	pressure
\mathbf{p}	=	separation or attachment point
\mathbf{q}	=	separation or attachment point
R	=	gas constant
Re	=	Reynolds number
S	=	step-height dimension
\mathcal{S}	=	separation surface
T	=	temperature
u	=	velocity in the x direction
\mathbf{u}	=	velocity tangential to the boundary
v	=	velocity in the y direction
\mathbf{v}	=	three-dimensional steady velocity field
W	=	spanwise width dimension
w	=	velocity in the z direction
\mathbf{x}	=	spatial coordinate vector
x	=	spatial coordinate
y	=	spatial coordinate
z	=	spatial coordinate
β	=	ratio of specific heats, c_p/c_v
Γ	=	unstable limit cycle
γ	=	boundary trajectory

θ	=	separation angle
κ	=	thermal conductivity
λ	=	first coefficient of viscosity
μ	=	second coefficient of viscosity
ν	=	kinematic viscosity
ρ	=	density
σ	=	stress tensor
τ	=	wall-shear field
ω	=	wall-vorticity field

Subscripts

f	=	reference property
x	=	derivative with respect to x
y	=	derivative with respect to y
z	=	derivative with respect to z
1	=	x direction
2	=	y direction
3	=	z direction

I. Introduction

THE accurate identification of separation patterns in three-dimensional flows is important for a number of engineering applications. For instance, separation and attachment has a major impact on mixing in combustors and on the aerodynamic forces acting on an aircraft, a submarine, or a passenger car. In several instances, the separation location itself is crucially important to detect. Drag reduction by wall-based flow control, for example, is known to be most effective when the actuators are placed close to separation surfaces.

The systematic study of steady-flow separation dates back to the seminal work of Prandtl [1] in 1904. He showed that a two-dimensional steady flow separates from a no-slip boundary at points at which the wall shear vanishes and admits a negative gradient. Three-dimensional flows, however, tend to separate along lines [2–6], as opposed to isolated wall-shear zeros.

In three dimensions, integral curves of the wall-shear vector field (also known as wall-shear lines or limiting streamlines) are the only viable candidates for separation lines, because they mark the intersection of two-dimensional stream surfaces with the boundary. Legendre [7] proposed to analyze wall-shear lines in topological terms used in the local theory of two-dimensional vector fields. In this topological approach, one tries to infer the global geometry of the

Received 29 November 2005; revision received 30 October 2006; accepted for publication 28 November 2006. Copyright © 2007 by the American Institute of Aeronautics and Astronautics, Inc. All rights reserved. Copies of this paper may be made for personal or internal use, on condition that the copier pay the \$10.00 per-copy fee to the Copyright Clearance Center, Inc., 222 Rosewood Drive, Danvers, MA 01923; include the code 0001-1452/07 \$10.00 in correspondence with the CCC.

*Graduate Assistant, Department of Mechanical Engineering.

†Assistant Professor, Department of Aerospace Engineering and Engineering Mechanics. Member AIAA.

‡Professor, Department of Mechanical Engineering; ghaller@mit.edu (Corresponding Author).

wall-shear field from local analysis near critical points. In [8–11], Legendre’s theory is further discussed and refined.

Lighthill [12] offered a more global view by proposing the convergence of wall-shear lines as a necessary criterion for separation. He concluded that separation lines always connect saddle points of the wall-shear field to stable spirals or nodes. In some flows [13], however, the separation lines defy this paradigm. For example, in flows past spheroids [13], the separation line appears to originate from a regular point.

Wu et al. [14] proposed to look beyond skin-friction patterns and view separation as distinguished three-dimensional particle motion near the boundary. These authors defined the separation surface as a two-dimensional set of fluid trajectories backward-asymptotic to a saddle-type wall-shear zero. For the three-dimensional boundary-layer equations, Van Dommelen and Cowley [15] also took a particle-based view by defining separation as a formation of a material spike that leaves the boundary layer. Still in the Lagrangian context, Wu et al. [16] derived conditions for the simultaneous convergence and upwelling of fluid near the boundary.

Despite the preceding advances, identifying exact separation and attachment locations in three-dimensional steady flows has remained a challenge. Converging or diverging wall-shear lines are indicators of separation or attachment, but tend to fill open regions of the boundary. For this reason, heuristic indicators such as zero wall shear [17] or zero streamwise wall shear [18,19] are commonly used to extract a single separation line candidate. These indicators are known to be inaccurate, but are still convenient choices for benchmarking, as noted by Nie and Armaly [20].

Another challenge is the identification of the two-dimensional separation surface (often called a shear layer) that emanates from the separation line. Although several studies noted different particle behaviors on different sides of inferred separation surfaces [17,21,22], no tools were available to extract such surfaces from numerical or experimental data. As a result, the global geometry of separated flows has only been studied thoroughly in two-dimensional cross sections or along individual streamlines.

Recently, Surana et al. [23] developed an exact theory of three-dimensional steady separation to address the preceding challenges. Based on nonlinear dynamic systems techniques, the theory gives mathematical criteria for the location of one- and two-dimensional unstable manifolds emanating from the wall. The unstable manifolds collect and eject particles from arbitrarily small neighborhoods of the wall and hence are the Lagrangian objects responsible for separation. Stable manifolds act in the same way in backward time and hence are the Lagrangian objects responsible for attachment.

Surprisingly, only four basic manifold topologies may exist, as shown in [23]. The theory also provides a first-order approximation for separation and attachment surfaces near the wall. The resulting formula for the location of these surfaces only depends on the wall shear; the formula for the slope of the surfaces depends on the wall shear, the wall-pressure gradient, the wall density, and the wall viscosity.

Here, we provide the first application of the preceding separation theory to direct numerical simulations of three-dimensional steady flows over a backward-facing step and in a lid-driven cavity. Computing all necessary formulas of the theory, we identify all one- and two-dimensional separation and attachment locations. We also determine local tangent approximations to the separation surfaces and then find the global separation surfaces by advecting the local approximations. Our analysis follows a well-defined wall-based algorithm, thus the present study of two specific benchmark problems also provides a practical recipe to uncover the geometry of three-dimensional steady separated flows.

In Sec. II, we review the theory from Surana et al. [23]. In Sec. III, we describe the numerical model and simulation of the backward-facing-step and lid-driven-cavity flows. In Sec. IV, we apply the exact separation theory to these flows to identify all separation lines and surfaces. The final section is reserved for conclusions and a description of related work on open separation and unsteady separation.

II. Separation in Three-Dimensional Steady Flows

A. Setup and Notation

Consider a three-dimensional steady velocity field

$$\mathbf{v}(x, y, z) = [u(x, y, z), v(x, y, z), w(x, y, z)] \quad (1)$$

that satisfies the steady continuity equation

$$\nabla \cdot (\rho \mathbf{v}) = 0 \quad (2)$$

with the fluid density $\rho(x, y, z)$.

For simplicity, assume that there is a flat boundary (i.e., a two-dimensional plane) at $z = 0$, where the velocity field \mathbf{v} satisfies the no-slip boundary condition:

$$u(\mathbf{x}, 0) = v(\mathbf{x}, 0) = w(\mathbf{x}, 0) = 0 \quad (3)$$

Fluid particles (i.e., infinitesimal volumes of fluid moving along trajectories $\mathbf{x}(t) = [x(t), y(t), z(t)]$) are advected by the Lagrangian equations of particle motion:

$$\dot{\mathbf{x}} = \mathbf{v}(\mathbf{x}) \quad (4)$$

All notions of stability and instability used in this paper would be with respect to the trajectories generated by Eq. (4).

We note that the separation and attachment criteria we discuss here extend to general curved boundaries, as described in [23]. In our notation, we distinguish the velocity components parallel to the boundary by letting

$$\begin{aligned} \mathbf{x} &= (x, y), & \mathbf{u}(\mathbf{x}, z) &= [u(x, y, z), v(x, y, z)] \\ w(\mathbf{x}, z) &= w(x, y, z) \end{aligned}$$

The *wall-shear* field on the boundary is defined as

$$\boldsymbol{\tau}(\mathbf{x}) = \partial_z \mathbf{u}(\mathbf{x}, 0) \quad (5)$$

Another quantity of interest is the *wall-vorticity* field

$$\boldsymbol{\omega}(\mathbf{x}) = \partial_z \mathbf{u}^\perp(\mathbf{x}, 0) \quad (6)$$

where $(a, b)^\perp = (-b, a)$.

If $\mathbf{x}(s, \mathbf{x}_0)$ denotes a trajectory of the wall-shear field $\boldsymbol{\tau}(\mathbf{x})$ with $\mathbf{x}(s, \mathbf{x}_0) = \mathbf{x}_0$, then

$$\partial_z^2 w(s) = \partial_z^2 w[\mathbf{x}(s, \mathbf{x}_0), 0] \quad (7)$$

measures the flow-stretching rate normal to the wall along $\mathbf{x}(s, \mathbf{x}_0)$. Using Eq. (3) in the continuity equation (2), we can express $\partial_z^2 w(\mathbf{x}, 0)$ from wall-based quantities as

$$\partial_z^2 w(\mathbf{x}, 0) = -\nabla_{\mathbf{x}} \cdot \boldsymbol{\tau}(\mathbf{x}) - \frac{1}{\rho(\mathbf{x}, 0)} \nabla_{\mathbf{x}} \rho(\mathbf{x}, 0) \cdot \boldsymbol{\tau}(\mathbf{x}) \quad (8)$$

B. Separation and Attachment Definitions

We say that the flow separates at the $z = 0$ boundary if fluid particles starting arbitrarily close to the boundary converge to a streamline \mathcal{L} (separation curve) or a stream surface \mathcal{S} (separation surface), along which they are ejected from the boundary (see Fig. 1). In the language of nonlinear dynamics, \mathcal{L} is a one-dimensional unstable manifold of a boundary point (separation point) and \mathcal{S} is a two-dimensional unstable manifold of a curve of boundary points (separation line).

We define attachment as separation exhibited by the flow in backward time. Attachment points are, therefore, boundary points with a one-dimensional stable manifold (attachment curve), and attachment lines are boundary curves with a two-dimensional stable manifold (attachment surface), as shown in Fig. 2.

We shall focus on separation and attachment surfaces and lines that are bounded, smooth, locally unique, transverse to the boundary, and robust with respect to small perturbations to the flow. For such

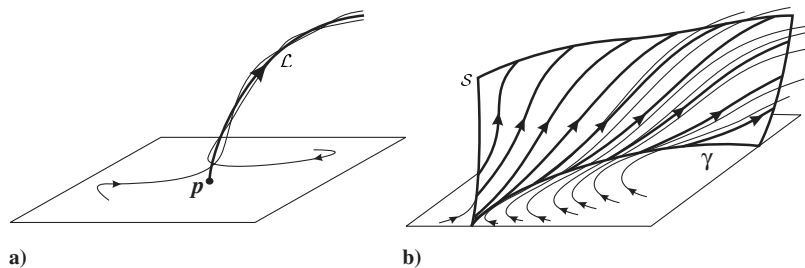


Fig. 1 Steady separation along a) a streamline (one-dimensional unstable manifold) \mathcal{L} and b) a stream surface (two-dimensional unstable manifold) \mathcal{S} .

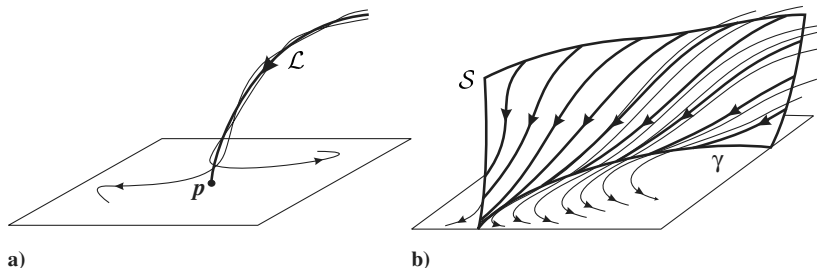


Fig. 2 Steady attachment along a) a streamline (one-dimensional stable manifold) \mathcal{L} and b) a stream surface (two-dimensional stable manifold) \mathcal{S} .

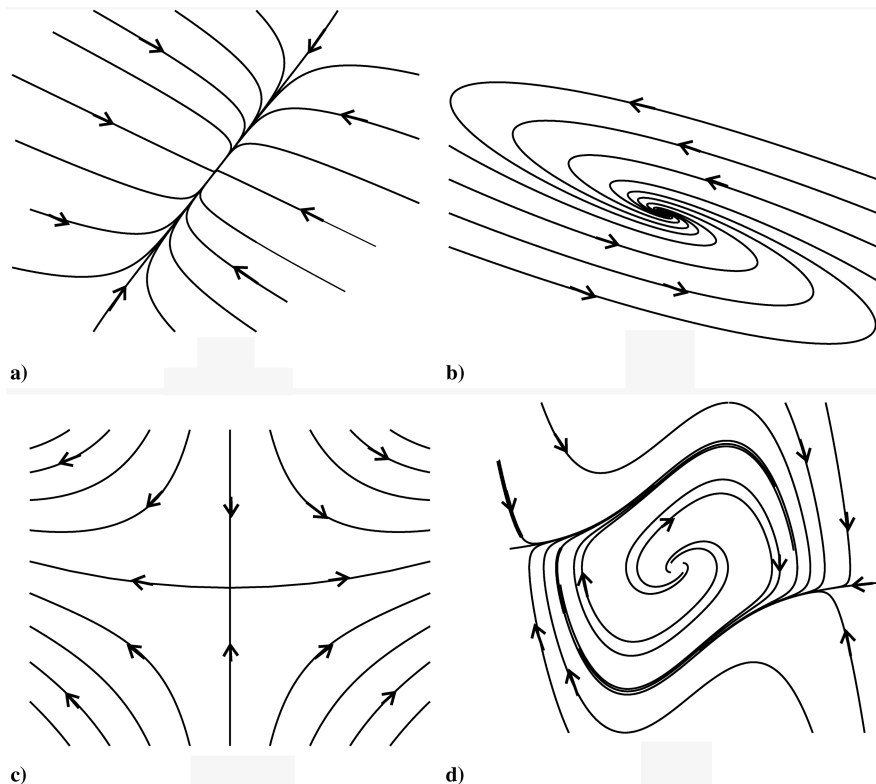


Fig. 3 The main planar vector field features used in our discussion: a) node, b) spiral, c) saddle, and d) stable limit cycle.

structures, a mathematically exact nonlinear theory was developed in [23], which we shall review next.

C. Separation and Attachment Criteria

For what follows, we first recall in Fig. 3 the basic topology of fixed points and limit cycles we are going to use in the following discussion. In [23] it was shown that if \mathbf{p} is a point on the $z = 0$ boundary, then

$S0 \mathbf{p}$ is a separation point if, and only if,

$$\tau(\mathbf{p}) = 0, \quad \nabla_x \cdot \tau(\mathbf{p}) < 0, \quad \det \nabla_x \tau(\mathbf{p}) > 0 \quad (9)$$

that is, \mathbf{p} is either a stable node or a stable spiral of the wall-shear field (5).

$R0 \mathbf{p}$ is an attachment point if, and only if,

$$\tau(\mathbf{p}) = 0, \quad \nabla_x \cdot \tau(\mathbf{p}) > 0, \quad \det \nabla_x \tau(\mathbf{p}) > 0$$

that is, \mathbf{p} is either a unstable node or a unstable spiral of the wall-shear field (5).

As argued in [23], a separation or attachment line γ is necessarily a full wall-shear trajectory $\{\mathbf{x}(s, \mathbf{x}_0)\}_{s=0}^{\infty}$. Because there are infinitely many wall-shear trajectories on the $z = 0$ boundary, additional criteria are required to identify separation and attachment lines. The

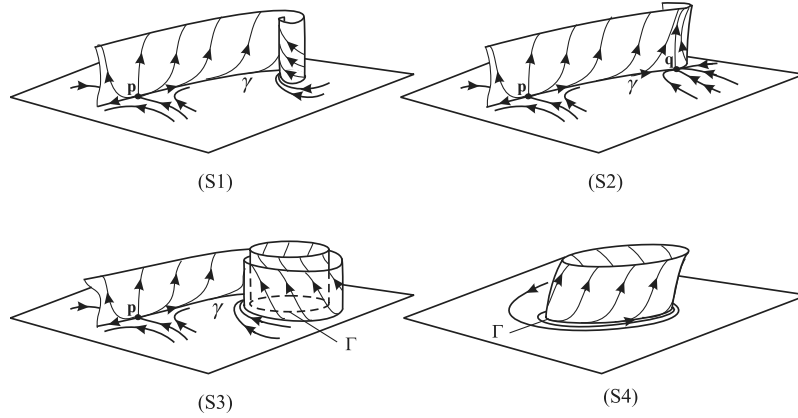


Fig. 4 Four basic separation patterns S1–S4.

following criterion provides sufficient and necessary conditions for the existence of such lines.

1. Separation Line Criterion

A bounded trajectory γ of the wall-shear field is a separation line if, and only if, one of the following holds (cf. Fig. 4):

1) S1 γ originates from a saddle \mathbf{p} with $\nabla_{\mathbf{x}} \cdot \boldsymbol{\tau}(\mathbf{p}) < 0$ and ends at a stable spiral \mathbf{q} with $\nabla_{\mathbf{x}} \cdot \boldsymbol{\tau}(\mathbf{q}) < 0$.

2) S2 γ originates from a saddle \mathbf{p} with $\nabla_{\mathbf{x}} \cdot \boldsymbol{\tau}(\mathbf{p}) < 0$ and ends at a stable node \mathbf{q} with $\nabla_{\mathbf{x}} \cdot \boldsymbol{\tau}(\mathbf{q}) < 0$. Also, γ is tangent to the direction of weaker attraction at \mathbf{q} .

3) S3 γ originates from a saddle \mathbf{p} with $\nabla_{\mathbf{x}} \cdot \boldsymbol{\tau}(\mathbf{p}) < 0$ and spirals onto a stable limit cycle Γ with

$$\int_{\Gamma} \nabla_{\mathbf{x}} \cdot \boldsymbol{\tau}[\mathbf{x}(s; \mathbf{x}_0)] ds < 0$$

4) S4 γ is a stable limit cycle with

$$\int_{\gamma} \nabla_{\mathbf{x}} \cdot \boldsymbol{\tau}(s; \mathbf{x}_0) ds < 0$$

In general, combinations of the basic separation patterns S1–S3 are also possible. Two examples are shown in Fig. 5: the first shows separation lines connecting a saddle to a node and a spiral; the second shows two separation lines emanating from different saddles but approaching the same spiral.

2. Attachment Line Criterion

A bounded trajectory γ of the wall-shear field is an attachment line if, and only if, one of the following holds:

1) R1 γ originates from an unstable spiral \mathbf{p} , where $\nabla_{\mathbf{x}} \cdot \boldsymbol{\tau}(\mathbf{p}) > 0$ and ends at a saddle \mathbf{q} , where $\nabla_{\mathbf{x}} \cdot \boldsymbol{\tau}(\mathbf{q}) > 0$.

2) R2 γ originates from an unstable node \mathbf{p} with $\nabla_{\mathbf{x}} \cdot \boldsymbol{\tau}(\mathbf{p}) > 0$ and ends at a saddle \mathbf{q} with $\nabla_{\mathbf{x}} \cdot \boldsymbol{\tau}(\mathbf{q}) > 0$. Also, γ is tangent to the direction of weaker repulsion at \mathbf{p} .

3) R3 γ spirals off from an unstable limit cycle Γ with

$$\int_{\Gamma} \nabla_{\mathbf{x}} \cdot \boldsymbol{\tau}[\mathbf{x}(s; \mathbf{x}_0)] ds > 0$$

and ends at a saddle \mathbf{q} with $\nabla_{\mathbf{x}} \cdot \boldsymbol{\tau}(\mathbf{q}) > 0$.

4) R4 γ is an unstable limit cycle with

$$\int_{\gamma} \nabla_{\mathbf{x}} \cdot \boldsymbol{\tau}[\mathbf{x}(s; \mathbf{x}_0)] ds > 0$$

The four basic attachment patterns R1–R4 and their combinations can be visualized by reversing the arrows in Figs. 4 and 5.

All saddles, nodes, spirals and limit cycles featured in the preceding separation and attachment criteria must be *nondegenerate*, that is, must attract or repel nearby wall-shear trajectories

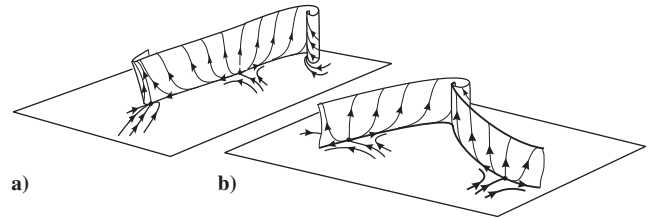


Fig. 5 Separation lines a) S1 and S2, emanating from the same saddle-type wall-shear zero and b) two S2, terminating at the same spiral-type wall-shear zero.

exponentially in s . Additionally, in the case of a node, the two rates of attraction or repulsion must be unequal.

Specifically, a nondegenerate node \mathbf{p} satisfies [23]

$$[\nabla_{\mathbf{x}} \cdot \boldsymbol{\tau}(\mathbf{p})]^2 > 4 \det \nabla_{\mathbf{x}} \boldsymbol{\tau}(\mathbf{p}) > 0 \tag{10}$$

a nondegenerate saddle \mathbf{p} satisfies

$$\det \nabla_{\mathbf{x}} \boldsymbol{\tau}(\mathbf{p}) < 0 \tag{11}$$

a nondegenerate spiral \mathbf{p} satisfies

$$0 < [\nabla_{\mathbf{x}} \cdot \boldsymbol{\tau}(\mathbf{p})]^2 < 4 \det \nabla_{\mathbf{x}} \boldsymbol{\tau}(\mathbf{p})$$

and a nondegenerate limit cycle Γ satisfies

$$\int_{\Gamma} \frac{\boldsymbol{\omega} \cdot (\nabla_{\mathbf{x}} \boldsymbol{\tau} \boldsymbol{\omega})}{|\boldsymbol{\omega}|^2} \Big|_{\mathbf{x}=\mathbf{x}(s, \mathbf{x}_0)} ds \neq 0 \tag{12}$$

D. Separation and Attachment at the Corners

The conditions in Eqs. (10–12) will hold for general flows as long as \mathbf{p} and γ are bounded away from the corners. Flows that separate or reattach at the corners, however, will violate Eq. (10) or Eq. (11); examples include the backward-facing-step flow and the lid-driven-cavity flow analyzed in this paper.

To see this, consider the case of a vertical wall satisfying $x = 0$ in Fig. 6. Because of the no-slip condition on the $z = 0$ and $x = 0$ planes, the velocity field can be written as [23]

$$\mathbf{v}(\mathbf{x}, z) = (x^2 z A, x z B, x z^2 C) \tag{13}$$

where

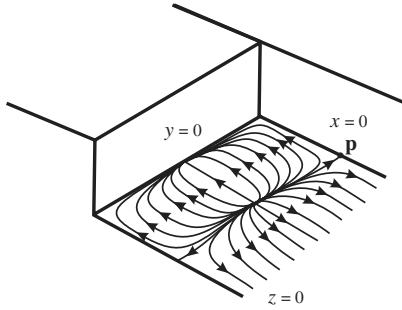


Fig. 6 Separation at the corners.

$$\begin{aligned}
 A(\mathbf{x}, z) &= \int_0^1 \int_0^1 \int_0^1 \partial_{xzx}^3 u(rqx, y, sz) q \, dq \, dr \, ds \\
 B(\mathbf{x}, z) &= \int_0^1 \int_0^1 \partial_{xz}^2 v(rx, y, sz) \, ds \, dr \\
 C(\mathbf{x}, z) &= \int_0^1 \int_0^1 \int_0^1 \partial_{xzz}^3 w(sx, y, rqz) q \, dq \, dr \, ds
 \end{aligned} \tag{14}$$

Consequently, the wall-shear field on the $z = 0$ boundary, its divergence, and the determinant of its gradient vanish identically at the corner formed by the intersection of $x = 0$ and $z = 0$.

Following [23], we now discuss higher-order analogs of the nondegeneracy conditions in Eqs. (10) and (11) under which S1–S4 and R1–R4 remain applicable at the corners. As we show in the Appendix, a point \mathbf{p} lies in the intersection of a wall-shear line and the $x = z = 0$ corner if

$$\partial_{xz}^2 v(\mathbf{p}, 0) = 0$$

We further show that the leading-order stretching rate off the $z = 0$ plane at the point \mathbf{p} is now given by

$$\partial_{xzz}^3 w(\mathbf{p}, 0) = -\nabla_{\mathbf{x}} \cdot \partial_x \boldsymbol{\tau}(\mathbf{p}) \tag{15}$$

A comparison of Eqs. (8) and (15) reveals that $\boldsymbol{\tau}$ must be replaced by $\partial_x \boldsymbol{\tau}$ in all conditions on nodes and saddles in S1–S3 and R1–R3. In addition, Eqs. (10) and (11) are replaced by the following two conditions: \mathbf{p} is a nondegenerate node if

$$[\nabla_{\mathbf{x}} \cdot \partial_x \boldsymbol{\tau}(\mathbf{p})]^2 > 4 \det \nabla_{\mathbf{x}} \partial_x \boldsymbol{\tau}(\mathbf{p}) > 0 \tag{16}$$

whereas \mathbf{p} is a nondegenerate saddle if

$$\det \nabla_{\mathbf{x}} \partial_x \boldsymbol{\tau}(\mathbf{p}) < 0 \tag{17}$$

E. Separation and Attachment Slope

If \mathbf{p} is a separation point, the one-dimensional separation curve \mathcal{L} emanating from \mathbf{p} is locally represented by

$$\mathbf{x} = \mathbf{p} + z\mathbf{G}(z) \tag{18}$$

where \mathbf{G} admits the Taylor-series expansion

$$\mathbf{G}(z) = \mathbf{g}_0 + z\mathbf{g}_1 + \frac{1}{2}z^2\mathbf{g}_2 + \frac{1}{6}z^3\mathbf{g}_3 + \dots \tag{19}$$

The slope of \mathcal{L} obeys the formula [23]

$$\mathbf{g}_0 = -\{2\nabla_{\mathbf{x}} \boldsymbol{\tau}(\mathbf{p}) + [\nabla_{\mathbf{x}} \cdot \boldsymbol{\tau}(\mathbf{p})]\mathbf{I}\}^{-1} \partial_z^2 \mathbf{u}(\mathbf{p}, 0) \tag{20}$$

with \mathbf{I} denoting the two-dimensional identity matrix; the same formula is valid for attachment curves. The higher-order terms in Eq. (19) are obtained from a recursive scheme.

Similarly, if γ is a separation line, then the corresponding two-dimensional separation surface \mathcal{S} and the wall normal at a point $\mathbf{x}_0 \in \gamma$ encloses an angle $\theta(\mathbf{x}_0)$ that satisfies

$$\tan \theta(\mathbf{x}_0) = - \lim_{s \rightarrow -\infty} \int_0^s \int_0^r e^{\int_0^q (\partial_z^2 w(q) - S_{\perp}(q)) \, dq} \frac{\partial_z^2 \mathbf{u} \cdot \boldsymbol{\omega}}{2|\boldsymbol{\omega}|} \Big|_{\mathbf{x}=\mathbf{x}(r, \mathbf{x}_0), z=0} \, dr \tag{21}$$

where $\partial_z^2 w(q)$ is defined in Eq. (7), and $S_{\perp}(q)$ is defined as

$$S_{\perp}(q) = \frac{\boldsymbol{\omega} \cdot (\nabla_{\mathbf{x}} \boldsymbol{\tau} \boldsymbol{\omega})}{|\boldsymbol{\omega}|^2} \Big|_{\mathbf{x}=\mathbf{x}(q, \mathbf{x}_0)}$$

measuring the wall-shear stretching rate normal to $\mathbf{x}(q, \mathbf{x}_0)$. Attachment angles can be computed by changing the limit to $s \rightarrow +\infty$ in Eq. (21).

F. Separation in Navier–Stokes Flows

In flows governed by the Navier–Stokes equations, the separation slope and angle formulas can be simplified to depend on on-wall quantities only. To illustrate this, we consider the general compressible Navier–Stokes momentum equations

$$\frac{\partial(\rho \mathbf{v})}{\partial t} + \nabla \cdot (\rho \mathbf{v} \mathbf{v}) = -\nabla p + \nabla \cdot \boldsymbol{\sigma} \tag{22}$$

with $\mathbf{v} \mathbf{v}$ denoting the dyadic product of \mathbf{v} with itself. The stress tensor $\boldsymbol{\sigma}$ is given by

$$\boldsymbol{\sigma} = \lambda(\nabla \cdot \mathbf{v})\mathbf{I} + 2\mu\mathbf{D}$$

where \mathbf{I} is 3×3 and $\mathbf{D} = \frac{1}{2}[\nabla \mathbf{v} + (\nabla \mathbf{v})^T]$. Invoking the Stokes hypothesis $3\lambda + 2\mu = 0$, we rewrite the stress tensor in component form as

$$\sigma_{ij} = -\frac{2}{3}\mu \frac{\partial v_k}{\partial x_k} \delta_{ij} + \mu \left[\frac{\partial v_i}{\partial x_j} + \frac{\partial v_j}{\partial x_i} \right] \tag{23}$$

with δ_{ij} denoting the Kronecker delta, with $(x_1, x_2, x_3) \equiv (\mathbf{x}, z)$ and $\mathbf{v} = (v_1, v_2, v_3) \equiv (u, v, w)$, and with summation understood over repeated indices.

Under the assumption that the viscosity coefficients are constant and the flow is steady, Eq. (22) becomes

$$\frac{\partial(\rho v_i v_j)}{\partial x_j} = -\frac{\partial p}{\partial x_i} + \mu \frac{\partial \sigma_{ij}}{\partial x_j} \tag{24}$$

Consider the x_1 component of Eq. (24),

$$\frac{\partial(\rho u u)}{\partial x} + \frac{\partial(\rho u v)}{\partial y} + \frac{\partial(\rho u w)}{\partial z} = -\frac{\partial p}{\partial x} + \mu \left[\frac{\partial \sigma_{xx}}{\partial x} + \frac{\partial \sigma_{xy}}{\partial y} + \frac{\partial \sigma_{xz}}{\partial z} \right] \tag{25}$$

Note that on the boundary $x_3 \equiv z = 0$, we have

$$\begin{aligned}
 \frac{\partial(\rho u u)}{\partial x} + \frac{\partial(\rho u v)}{\partial y} + \frac{\partial(\rho u w)}{\partial z} &= 0, & \frac{\partial \sigma_{xx}}{\partial x} &= 0 \\
 \frac{\partial \sigma_{xy}}{\partial y} &= 0, & \frac{\partial \sigma_{xz}}{\partial z} &= \frac{\partial^2 u}{\partial z^2}
 \end{aligned}$$

which, coupled with Eq. (25), yields

$$u_{zz}(\mathbf{x}, 0) = \frac{1}{\mu} p_x(\mathbf{x}, 0)$$

A similar equation can be derived for the x_2 component. Combining the equations for the x_1 component and x_2 component leads to the relationship

$$\partial_z^2 \mathbf{u}(\mathbf{x}, 0) = \frac{1}{\rho \nu} \nabla_x p(\mathbf{x}, 0) \tag{26}$$

Given Eq. (26), the separation slope formula (20) and the separation angle formula (21) become

$$\mathbf{g}_0 = -\frac{1}{\rho v} [2\nabla_{\mathbf{x}} \boldsymbol{\tau}(\mathbf{p}) + \nabla_{\mathbf{x}} \cdot \boldsymbol{\tau}(\mathbf{p}) \mathbf{I}]^{-1} \nabla_{\mathbf{x}} p(\mathbf{p}, 0) \quad (27)$$

and

$$\begin{aligned} & \tan \theta(\mathbf{x}_0) \\ &= -\frac{1}{2\rho v} \lim_{s \rightarrow -\infty} \int_0^s e^{\int_0^r [\frac{1}{2} \partial_z^2 w(q) - S_{\perp}(q)] dq} \frac{(\nabla_{\mathbf{x}} p, \boldsymbol{\omega})}{|\boldsymbol{\omega}|} \Big|_{\mathbf{x}=\mathbf{x}(r, \mathbf{x}_0), z=0} \end{aligned} \quad (28)$$

Recall that $\partial_z^2 w(q)$ can be computed from on-wall quantities using Eq. (8). Attachment slopes and angles satisfy Eqs. (27) and (28) (with $s \rightarrow +\infty$).

G. Algorithm for Locating Separation and Attachment

The preceding results lead to the following algorithm for locating separation and attachment:

1) For a given wall-shear field $\boldsymbol{\tau}(\mathbf{x})$, find all nondegenerate zeros \mathbf{p}_i and limit cycles Γ_j . Away from the corners, use the conditions in Eqs. (10–12); at the corners, use Eqs. (16) and (17).

2) For the preceding \mathbf{p}_i and Γ_j , determine the sign of $\nabla_{\mathbf{x}} \cdot \boldsymbol{\tau}(\mathbf{p}_i)$ and

$$\int_{\Gamma_j} \nabla_{\mathbf{x}} \cdot \boldsymbol{\tau}[\mathbf{x}(s; \mathbf{x}_0)] ds$$

At the corners, determine the sign of $\nabla_{\mathbf{x}} \cdot \partial_x \boldsymbol{\tau}(\mathbf{p}_i)$, where x is the coordinate introduced in Sec. II.D along the corner line.

3) For each nondegenerate wall-shear saddle \mathbf{p}_k , find its stable and unstable manifolds in the $z = 0$ plane. The manifold $W^u(\mathbf{p}_k)$ is obtained numerically by advecting a small line segment (initially tangent to the unstable eigenvector of \mathbf{p}_k) using the flow of $\dot{\mathbf{x}} = \boldsymbol{\tau}(\mathbf{x})$. In other words, we take an initial condition on the unstable eigenvector of \mathbf{p}_k sufficiently close to \mathbf{p}_k and solve the system $\dot{\mathbf{x}} = \boldsymbol{\tau}(\mathbf{x})$ for that initial condition. The manifold $W^s(\mathbf{p}_k)$ is obtained by backward-advecting a small line segment, initially tangent to the stable eigenvector of \mathbf{p}_k using the flow of $\dot{\mathbf{x}} = \boldsymbol{\tau}(\mathbf{x})$.

4) Identify separation and attachment points using the criteria S0 and R0.

5) Identify separation and attachment lines from the criteria S1–S4 and R1–R4. At the corners, use $\partial_x \boldsymbol{\tau}(\mathbf{p}_i)$ instead of $\boldsymbol{\tau}(\mathbf{p}_i)$ in S1–S3 and R1–R3.

6) Compute the slope of separation and attachment curves using Eq. (20) or Eq. (27).

7) Compute first-order approximations for attachment and separation surfaces from the angle formula in Eq. (21) or Eq. (28).

8) If the velocity field off the boundary is available, compute global separation and attachment surfaces by advecting their tangent planes (obtained from the first-order approximation in item 7) in the appropriate time direction.

III. Numerical Simulations

A. Numerical Methodology

We consider a Newtonian fluid with zero bulk viscosity. The kinetic viscosity μ , the conductivity κ , and the specific heats at constant pressure c_p and at constant volume c_v are assumed to be independent of the temperature. Under these hypotheses, the nondimensional governing equations expressing the conservation of mass, momentum, and energy in Cartesian coordinates x_i become

$$\frac{\partial \rho}{\partial t} + \frac{\partial(\rho v_i)}{\partial x_i} = 0 \quad (29)$$

$$\frac{\partial(\rho v_i)}{\partial t} + \frac{\partial(\rho v_i v_j)}{\partial x_j} = -\frac{\partial p}{\partial x_i} + \frac{1}{Re} \frac{\partial \sigma_{ij}}{\partial x_j} \quad (30)$$

$$\frac{\partial(\rho e)}{\partial t} + \frac{\partial(\rho e v_i)}{\partial x_i} = -\frac{\partial(p v_i)}{\partial x_i} + \frac{\partial(v_j \sigma_{ij})}{\partial x_j} + \frac{1}{(\beta - 1) M_f^2 Pr} \frac{\partial^2 T}{\partial x_i^2} \quad (31)$$

As before, v_i denotes the velocity field components, p is the mechanical pressure, and e denotes the sum of internal and kinetic energies. The stress tensor σ_{ij} is given in Eq. (23). Equations (29–31) are closed with the ideal gas law

$$p = \frac{\rho T}{\beta M_f^2}$$

so that

$$e = \frac{p}{\beta - 1} + \rho \frac{u_i^2}{2}$$

All variables are normalized by the reference length L_f , the density ρ_f , the velocity U_f , and the temperature T_f . The nondimensional numbers in the preceding equation are the Reynolds number $Re = \rho_f U_f L_f / \mu$, the Prandtl number $Pr = c_p \mu / \kappa$, and the reference Mach number $M_f = U_f / C$, where $C = \sqrt{\beta R T_f}$ is the speed of sound with gas constant R .

We solve Eqs. (29–31) with a staggered-grid multidomain spectral method. For a detailed description and validation of this method, we refer to [24,25].

B. Numerical Models

We consider two different flow geometries: a backward-facing step and a lid-driven cavity. Both are classic benchmark problems with complex separation and attachment topologies that are ideal for the validation of the separation criteria listed in Sec. II.

1. Backward-Facing Step

We consider the two-dimensional, closed, backward-facing-step flow studied by Gresho et al. [26], with a slight three-dimensional perturbation added in the periodic spanwise direction. The computational model is shown in Fig. 7a.

The upstream and downstream lengths from the step are L_u and L_d . Following [26], we take $S = h = 1$, $L_u = 1$, and $L_d = 34$. We take the spanwise width to be $W = 4$.

At the inflow, we specify the analytical velocity and temperature curve of a flow between two infinite parallel plates:

$$\begin{aligned} u_0(z) &= -6[(z - S)^2 - (z - S)] \\ T(z) &= T_{\text{wall}} + \left\{ \frac{3(\beta - 1)}{4Pr} [1 - (2(z - S) - 1)^4] \right\} \end{aligned} \quad (32)$$

To introduce three-dimensional features into the flow, we modify the inflow u velocity as

$$u(y, z) = u_0(z)[1 + 0.1 \cos(2\pi y/W)]$$

At the outflow, we again specify velocity and temperature profiles according to the analytical flow between parallel plates, so that the mass-flow rates at the inflow and outflow are equal. We compute the prescribed pressure difference between inflow and outflow from the analytical channel-flow pressure gradient. The walls are no-slip and isothermal; the spanwise boundary conditions are periodic. We initialize the flow with the inflow boundary condition (32).

The Reynolds number based on the bulk inflow velocity and the step height is $Re = 300$, ensuring laminar separation on the top wall [27]. The Mach number based on the wall temperature and the inflow bulk velocity is $Ma = 0.4$, which ensures a nearly incompressible flow without restricting the explicit-time-scheme step. The Prandtl number is $Pr = 0.72$.

The numerical studies of Armaly et al. [27] and Gresho et al. [26] indicate that at $Re = 300$, the backward-facing-step flow is two-dimensional. To generate three-dimensional effects, we therefore introduced an additional spatial spanwise variation in the inlet velocity field. Because the numerical methodology we used is similar to that described in [26], we adopt the resolution from that study. By taking the Reynolds number to be 25% less than used in [26], we

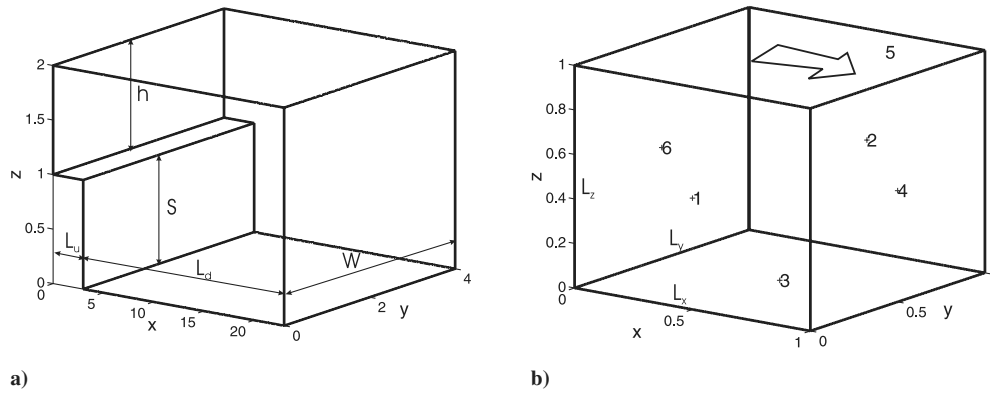


Fig. 7 Steady flow geometries studied in this paper: a) backward-facing step and b) lid-driven cavity.

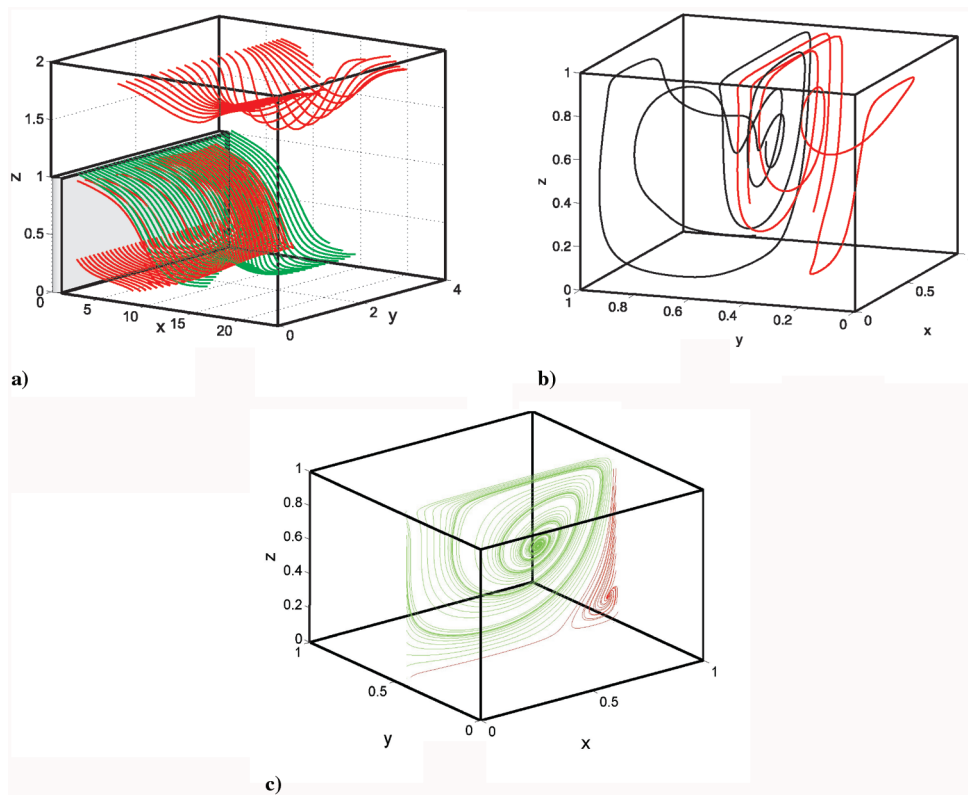


Fig. 8 Streamlines computed a) for the backward-facing step, b) for the lid-driven cavity, and c) in the $y = 0.5$ symmetry plane of the lid-driven cavity.

reasonably expect that the same resolution still guarantees convergence despite the new three-dimensional effects.

Specifically, we take 2×1 and 4×17 domains in the $x - z$ plane upstream and downstream of the sudden expansion. In accordance with the dimensions of the elements in the $x - z$ plane, we take six elements in the spanwise direction. In each domain, we employ a ninth-order discretization.

With this setup, the flow reaches steady state after 200 nondimensional time units. We reproduced the 2-D steady-state solution of Gresho et al. [26] at $Re = 400$ (not shown here). To ensure a laminar steady flow for 3-D flow with the perturbed inflow boundary condition, we consider the flow at a slightly smaller Reynolds number of $Re = 300$ in our 3-D simulation.

In Fig. 8a, we show representative streamlines computed in the sudden expansion of the backward-facing step.

The flow separates at the sharp edge of the expansion and reattaches further downstream at the bottom wall. The sudden expansion also creates a smaller separation bubble on the top wall behind the step. As a result of the spanwise sinusoidal inflow perturbation, the separation and attachment patterns show a spanwise three-dimensional variation, which we shall analyze next.

2. Lid-Driven Cavity Flow

Our second study is on the lid-driven cavity. The computational model (Fig. 7b) consists of a cube with sides L . The top wall in the z direction is driven at a constant velocity u in the x direction. All walls are no-slip and isothermal. The velocity distribution on the moving top wall is tapered to zero toward the sides according to a parabolic profile; this is to avoid velocity singularities at these locations.

The Reynolds number based on the top-wall velocity and the cube side is $Re = 400$, ensuring laminar flow [28]. The Mach number based on the wall temperature and the inflow bulk velocity is $Ma = 0.1$, rendering the flow practically incompressible; the Prandtl number is $Pr = 0.72$. Started from a quiescent state, the flow reaches steady state after 25 nondimensional time units.

The computational grid consists of four domains, with the grid refined near the walls. With each domain of seventh order, we obtain a converged solution that is in close agreement with the 2-D simulations in [29]. Based on the convergence studies by Jacobs et al. [25], this resolution guarantees a well-resolved cavity flow.

For the Reynolds number $Re = 400$, the $y = 0.5$ midplane is invariant (i.e., composed of streamlines), as found in [28]. Figure 8c shows the 2-D streamline pattern in the midplane, with the separation

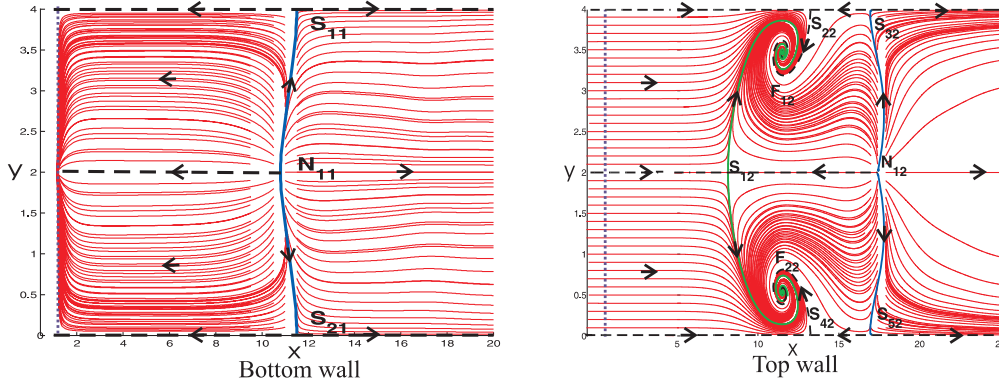


Fig. 9 Wall-shear lines computed on the top and bottom walls behind the backward-facing step. S_{ij} refer to saddles, N_{ij} to nodes, and F_{ij} to foci (spirals). We also indicate special wall-shear lines (stable and unstable manifolds of the saddles) connecting zeros. Among these, the solid lines will turn out to be actual separation lines (green) or attachment lines (blue). The location of step at $x = 1$ is indicated by a dotted magenta line.

and attachment clearly visible near the $x = 1$ wall. The streamlines in the cavity flow (Fig. 8b) exhibit complicated behavior [28], leading to the complex three-dimensional separation geometry that we identify next.

IV. Separation and Attachment Analysis

A. Backward-Facing Step

Figure 9 shows the wall-shear patterns on the bottom and top walls of the backward-facing step. The flow is periodic in the spanwise direction, as reflected by the periodic spanwise wall-shear distribution.

We now apply steps 1–8 of the separation and attachment detection algorithm described in Sec. II.G.

1. Steps 1–3

In Table 1, we list all zeros of τ on the top and bottom walls, along with quantities that verify the nondegeneracy of these zeros (steps 1–2). We then determine (step 3) the stable and unstable manifolds of all the nondegenerate wall-shear saddles S_{ij} , featured in Fig. 9.

2. Steps 4 and 5

Based on Table 1, criteria S0–S4 and R0–R4 of Sec. II.C give the following results (cf. Sec. II.G):

For the bottom wall,

- 1) N_{11} satisfies R0 and hence is an attachment point.
- 2) The wall-shear lines connecting N_{11} to S_{11} and S_{21} satisfy R2 and hence form an attachment line.

For the top wall,

- 1) F_{12} and F_{22} satisfy S0 and hence are separation points.
- 2) N_{12} satisfies R0 and hence is an attachment point.
- 3) The wall-shear lines connecting S_{12} to F_{12} and F_{22} satisfy S1 and hence form a separation line. (Note, however, that the lines connecting S_{32} to F_{12} and F_{22} do not form a separation line.)
- 4) The wall-shear lines connecting N_{12} to S_{32} and S_{52} satisfy R2 and hence form an attachment line.

Table 1 Classification of wall-shear zeros for the backward-facing step

Wall-shear zero	Bottom wall ($z = 0$)		$\nabla_{\mathbf{x}} \cdot \boldsymbol{\tau}$	$\det \nabla_{\mathbf{x}} \boldsymbol{\tau}$
	(x, y) coordinates			
$S_{11} = S_{21}$	(11.49, 4.00), (11.49, 0.00)		1.00	-1.00
N_{11}	(10.79, 2.00)		2.96	1.72
Wall-shear zero	Top wall ($z = 2$)		$\nabla_{\mathbf{x}} \cdot \boldsymbol{\tau}$	$\det \nabla_{\mathbf{x}} \boldsymbol{\tau}$
	(x, y) coordinates			
S_{12}	(8.15, 2.00)		-0.54	-0.16
$S_{22} \equiv S_{32}$	(13.25, 4.00), (13.25, 0.00)		0.05	-0.02
$S_{32} \equiv S_{52}$	(17.09, 4.00), (17.09, 0.00)		0.12	-0.01
N_{12}	(17.42, 2.00)		0.68	0.11
$F_{12} \equiv F_{22}$	(11.58, 3.46)		-0.09	0.006

3. Steps 6 and 7

We obtain the local separation and attachment surfaces identified previously by computing the angle formula Eq. (28) at each point of the separation or attachment line. Figures 10a and 11a show the resulting local analytic approximations to the separation and attachment surfaces, with nearby streamlines validating the approximations. In this example, separation and attachment curves are contained in separation and attachment surfaces, respectively, hence we do not compute them separately.

4. Step 8

Figures 10b and 11b show the corresponding global separation and attachment surfaces, which we obtained by advecting trajectories starting from the local approximate surfaces.

B. Lid-Driven Cavity Flow

We study the wall-shear field on each of the walls shown in Fig. 12. Because of the symmetry of the flow with respect to the $y = 0.5$ plane, walls 1 and 2 admit identical wall-shear fields. We will again go through steps 1–8 of the algorithm presented in Sec. II.G.

1. Steps 1–3

In Table 2, we list all zeros of $\boldsymbol{\tau}$ on walls 1–4 and 6. We also list the quantities that verify the nondegeneracy of these zeros (steps 1 and 2). In step 3, we determine the stable and unstable manifolds of all the nondegenerate wall-shear saddles shown in Fig. 12. Note that wall 5 is not fixed and hence violates the assumption in Eq. (3). The corresponding wall-shear lines in Fig. 12, however, show that there is no separation or attachment on this wall.

2. Steps 4 and 5

Based on Table 2, the separation and attachment criteria of Sec. II.C give the following results (cf. Sec. II.G):

For walls 1 and 2,

- 1) F_{11} satisfies S0 and hence is a separation point.
- 2) F_{21} and N_{11} satisfy R0 and hence are attachment points.
- 3) The wall-shear lines connecting S_{11} to F_{11} and N_{113} satisfy S1 and S2, respectively, and hence form a separation line.
- 4) The wall-shear lines connecting S_{21} to F_{11} and N_{114} satisfy S1 and S2, respectively, and hence form a separation line.

For wall 3,

- 1) N_{23} and N_{33} satisfy S0 and hence are separation points.
- 2) N_{13} satisfies R0 and hence is an attachment point.
- 3) The wall-shear lines connecting N_{13} to S_{13} , S_{232} , S_{134} and S_{231} all satisfy R2 and hence form attachment lines.
- 4) The wall-shear line connecting N_{136} to S_{13} satisfies R2 and hence is an attachment line.

For wall 4,

- 1) N_{24} and N_{34} satisfy S0 and hence are separation points.
- 2) N_{14} satisfies R0 and hence is an attachment point.

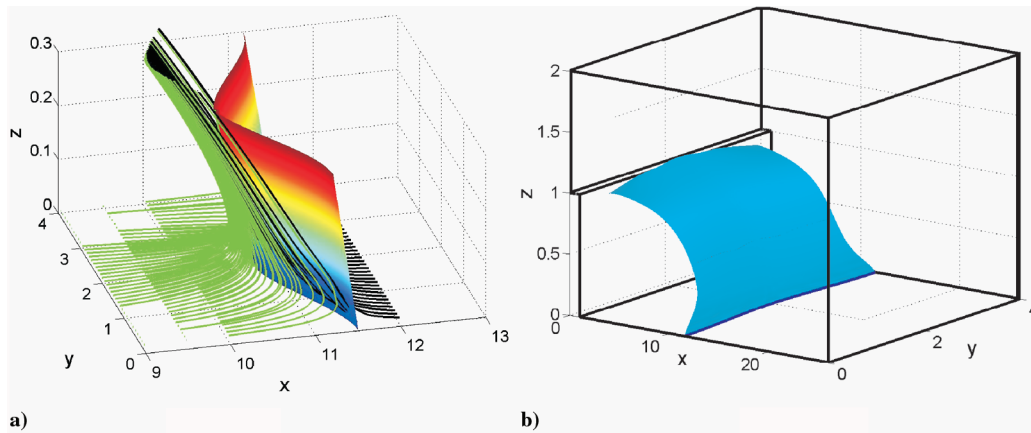


Fig. 10 Attachment surface on the bottom wall of the backward-facing step. a) Local analytic approximation validated by streamlines and b) global surface obtained from advecting the local approximation in time.

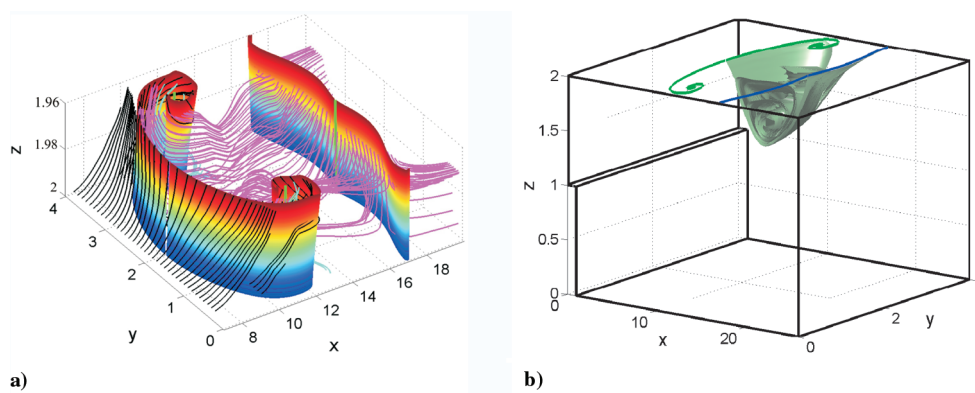


Fig. 11 Same as Fig. 10, but for the top wall. For better visibility, only half of the global separation surface is shown.

3) The wall-shear lines connecting S_{14} to N_{24} and N_{34} satisfy S2 and hence form a separation line.

4) The wall-shear line connecting N_{14} to S_{143} satisfies R2 and hence is an attachment line.

For wall 6,

1) N_{16} satisfies R0 and hence is an attachment point.

2) The wall-shear line connecting N_{16} to S_{161} and S_{162} satisfies R2 and hence is an attachment line.

3. Steps 6 and 7

Figures 13a, 14a, and 15a show the local analytic approximations to separation and attachment surfaces on walls 1, 3, and 4, respectively, along with nearby streamlines. Figure 16a shows the local analytic approximation to the attachment curve of the point N_{16} , along with nearby streamlines, obtained from Eq. (27). The wall-shear line connecting N_{16} to S_{161} and S_{162} represents an attachment line, but computing the first-order approximation to the corresponding separation surface would require a higher-order version of the angle formula (28), due to the corner degeneracy at S_{161} and S_{162} .

4. Step 8

Figures 13b, 14b, and 15b show the global separation and attachment surfaces obtained by advecting their local approximations in the appropriate time direction. Figure 16b shows the global attachment curve of N_{16} obtained by advecting the local attachment curve in backward time.

V. Conclusions

In this paper, we discussed a rigorous procedure for locating separation and attachment points and lines on fixed no-slip boundaries of three-dimensional steady fluid flows. The theoretical

foundations of this procedure are given in Surana et al. [23]; our focus was the application of the theory to direct numerical simulations of separated shear flows.

For Navier–Stokes flows, we relied on distributed measurements of the wall-shear field $\boldsymbol{\tau} = \partial_2 \mathbf{u}(\mathbf{x}, 0)$ to find the exact location of separation and attachment. Whenever the separation line is unique and bounded, the separation surface will be of one of the four topological types described in Sec. II.C. To obtain a tangent approximation for the separation and attachment structures, we also relied on distributed wall-pressure measurements.

As example flows, we considered a backward-facing step and a lid-driven cavity. In both examples, we gave a full analysis of the separation and attachment structures. In earlier studies [17–19] of these flows, only heuristic criteria such as those based on Prandtl’s 2-D separation conditions or visual inspection of tracings were used to characterize separation. In the present study, we systematically located the exact streamlines and stream surfaces to which fluid particles converge and depart from the wall. We also constructed the global separation and attachment surfaces by advecting their local approximations in the appropriate time direction. The resulting global surfaces have highly complex geometries that most likely result in chaotic streamlines.

The theory underlying our algorithm assumes the existence of a unique separation surface and hence is inapplicable to open separation or crossflow separation [5,30]. Nevertheless, appropriate extensions of the invariant manifold techniques yield a crossflow separation line and associated separation surface that best approximates the bulk of streamlines breaking away from the wall (Haller et al. [31]).

For three-dimensional unsteady flows with a well-defined asymptotic mean, separation and attachment lines can be detected by applying the present techniques to the time-averaged velocity field [32]. The separation lines then turn out to remain fixed in time, even though the corresponding separation surfaces are time-dependent.

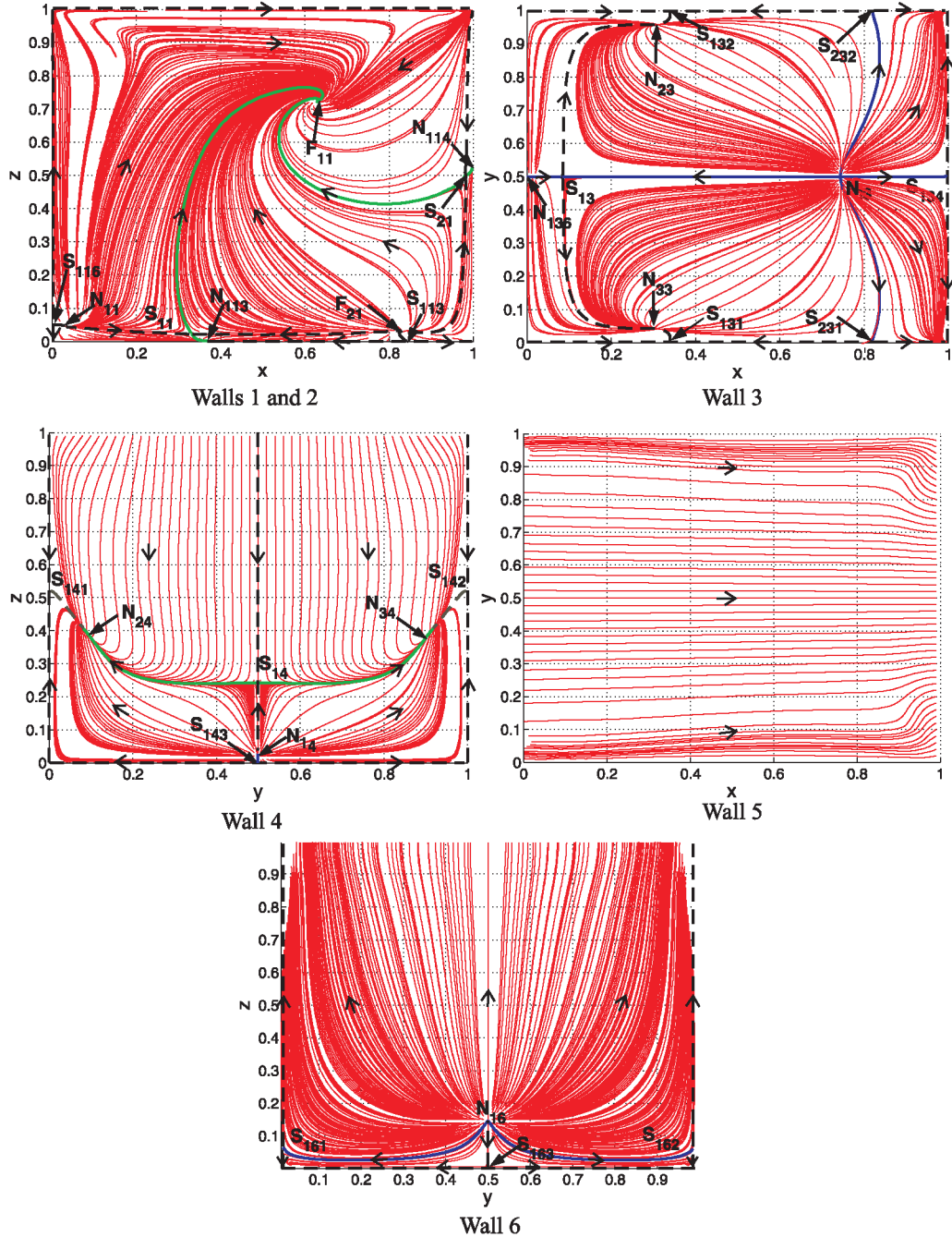


Fig. 12 Wall-shear fields on walls 1, 4, 5, and 6 for the lid-driven-cavity flow. We also indicate special wall-shear lines (stable and unstable manifolds of the saddles) connecting wall-shear zeros. Among these, the solid lines turn out to be actual separation lines (green) or attachment lines (blue) lines.

By contrast, the application of critical point theory to the instantaneous velocity field would suggest that the separation location is time-varying. For details of the time-dependent version of the present separation theory, we refer the reader to Surana et al. [32], who extend related two-dimensional results by Haller [33] and Kilic et al. [34].

Appendix

Using the form given in Eq. (13) for the velocity field and introducing the rescaled time s through the relation $ds/dt = x(t)z(t)$, we find that streamlines satisfy

$$\frac{d}{ds}(x, y, z) = (xA, B, zC) \tag{A1}$$

A point $\mathbf{p} = (0, p)$ in the $z = 0$ plane is a fixed point for Eq. (A1) if

$$B(\mathbf{p}, 0) = 0 \tag{A2}$$

To understand the topology of limiting streamlines near $(\mathbf{p}, 0)$, we linearize Eq. (A1) at $(\mathbf{p}, 0)$. The linearization of the scaled velocity field (A1) at $(\mathbf{p}, 0)$ admits the coefficient matrix:

$$\mathbf{M}(\mathbf{p}) = \begin{pmatrix} A(\mathbf{p}, 0) & 0 & 0 \\ \partial_x B(\mathbf{p}, 0) & \partial_y B(\mathbf{p}, 0) & \partial_z B(\mathbf{p}, 0) \\ 0 & 0 & C(\mathbf{p}, 0) \end{pmatrix} \tag{A3}$$

Restricted to the $z = 0$ plane, the eigenvalues of $\mathbf{M}(\mathbf{p})$ are

$$A(\mathbf{p}, 0) = \partial_{xxz}^3 u(\mathbf{p}, 0), \quad \partial_y B(\mathbf{p}, 0) = \partial_{xy^2z}^3 v(\mathbf{p}, 0) \tag{A4}$$

thus, \mathbf{p} can only be a saddle or a node for the rescaled Eq. (A1) within the $z = 0$ plane.

Table 2 Classification of wall-shear zeros for the lid-driven cavity. The third-order derivatives were obtained by spectral differentiation of the polynomial base functions [24]

	Wall 1 ($y = 0$) and Wall 2 ($y = 1$)	$\nabla_x \cdot \tau$	$\det \nabla_x \tau$
Wall-shear zero	(x, z)		
S_{11}	(0.33, 0.02)	-0.36	-0.74
S_{21}	(0.97, 0.50)	-3.99	-17.81
F_{11}	(0.63, 0.73)	-15.72	103.20
F_{21}	(0.83, 0.03)	1.78	0.87
N_{11}	(0.03, 0.05)	0.82	0.17
	Wall 1 ($y = 0$) corners and wall 2 ($y = 1$) corners	$\nabla_x \cdot \partial_x \tau$	$\det \nabla_x \partial_x \tau$
Wall-shear zero	(x, z)		
N_{114}, S_{141}	(1.00, 0.52)	-247.77	5076.68
S_{116}, S_{161}	(0.00, 0.05)	6.80	-434.07
	Wall 3 ($z = 0$)	$\nabla_x \cdot \tau$	$\det \nabla_x \tau$
Wall-shear zero	(x, y)		
S_{13}	(0.08, 0.50)	1.59	-5.00
N_{13}	(0.74, 0.50)	16.49	61.60
N_{23}	(0.31, 0.96)	-3.24	2.54
N_{33}	(0.03, 0.04)	-3.45	2.84
	Wall 3 ($z = 0$) corners	$\nabla_x \cdot \partial_y \tau$	$\det \nabla_x \partial_y \tau$
Wall-shear zero	(x, y)		
N_{113}, S_{131} or S_{132}	(0.34, 0.00) or (0.34, 1.00)	16.63	-3256.11
S_{113}, S_{231} or S_{232}	(0.83, 0.00) or (0.83, 1.00)	27.96	-81.12
	Wall 3 at intersections with wall 4 and 6	$\nabla_x \cdot \partial_x \tau$	$\det \nabla_x \partial_x \tau$
Wall-shear zero	(x, y)		
S_{134}, S_{143}	(1, 0.50)	3.30	-9219.04
N_{136}, S_{163}	(0, 0.50)	131.51	3180.26
	Wall 4 ($x = 1$)	$\nabla_x \cdot \tau$	$\det \nabla_x \tau$
Wall-shear zero	(y, z)		
S_{14}	(0.50, 0.24)	-3.89	-2.10
N_{14}	(0.50, 0.15)	8.03	15.90
N_{24}	(0.08, 0.41)	-7.24	9.09
N_{34}	(0.92, 0.41)	-7.15	8.36
	Wall 6 ($x = 0$)	$\nabla_x \cdot \tau$	$\det \nabla_x \tau$
Wall-shear zero	(y, z)		
N_{16}	(0.50, 0.15)	8.03	15.90

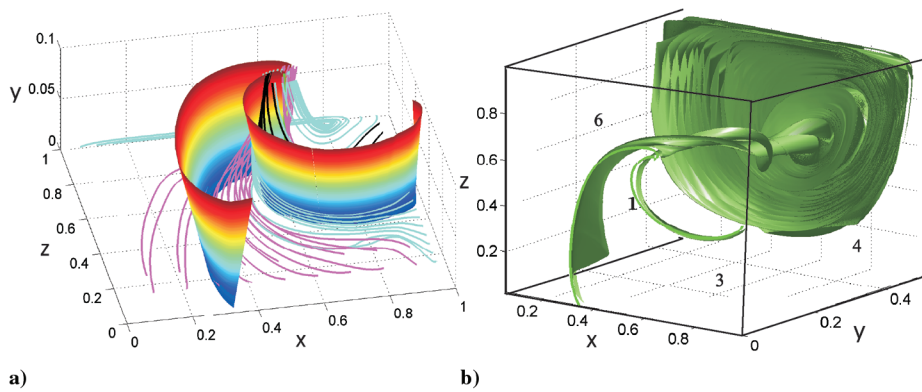


Fig. 13 Approximation to the separation surfaces a) local, for walls 1 and 2, obtained from the slope formula in Eq. (28) and b) global, obtained by advecting the local approximate surfaces in time.

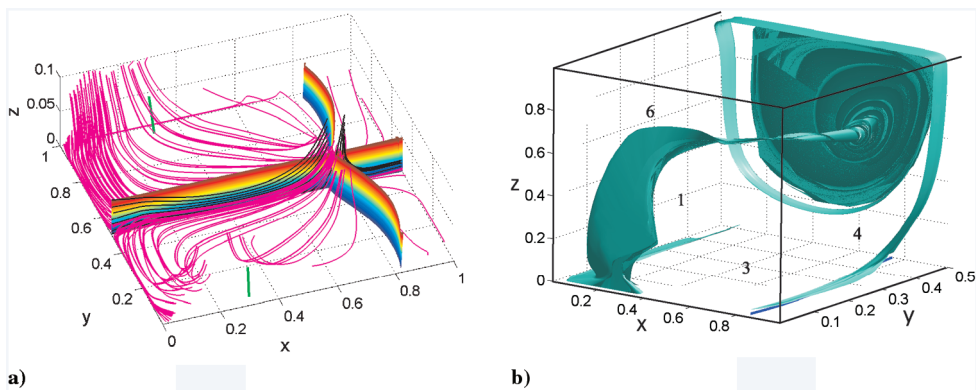


Fig. 14 Same as Fig. 13 but for wall 3.

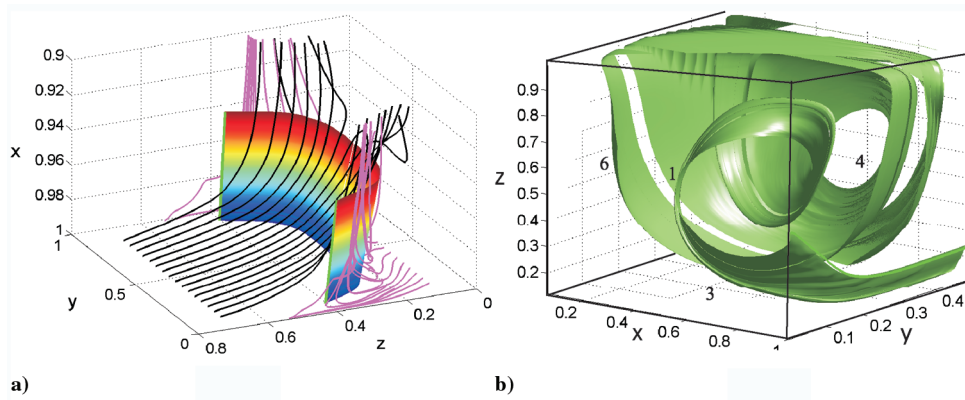


Fig. 15 Same as Fig. 13 but for wall 4.

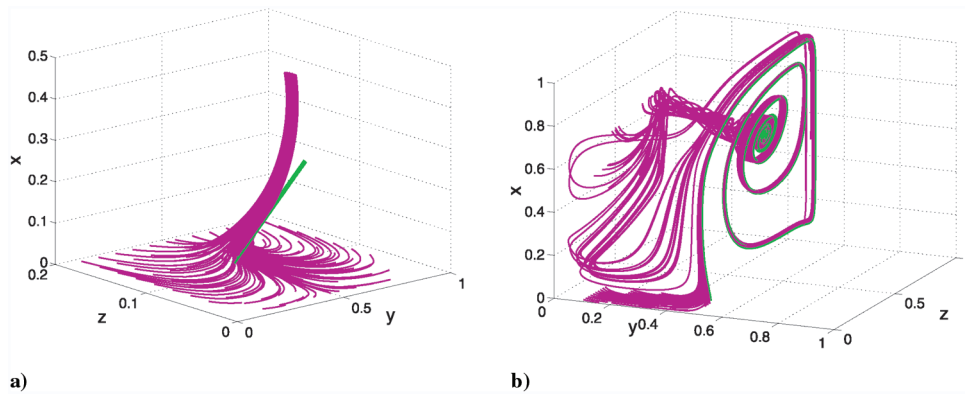


Fig. 16 Approximation to the attachment curve a) local, for wall 6, obtained from the slope formula (27) and b) global, obtained by advecting the local approximate curve in backward time, along with the nearby streamlines.

From the characteristic Eq. (A3), we find that \mathbf{p} is a nondegenerate node within the $z = 0$ plane in Eq. (A1) if

$$[A(\mathbf{p}, 0) + \partial_y B(\mathbf{p}, 0)]^2 > 4A(\mathbf{p}, 0)\partial_y B(\mathbf{p}, 0) > 0 \quad (\text{A5})$$

whereas \mathbf{p} is a nondegenerate saddle within the $z = 0$ plane if

$$A(\mathbf{p}, 0)\partial_y B(\mathbf{p}, 0) < 0 \quad (\text{A6})$$

Combining Eqs. (A5) and (A6) with Eq. (A4) gives the nondegeneracy conditions in Eqs. (16) and (17).

Using the form in Eq. (13) for the velocity field in the continuity equation (2), we obtain

$$\begin{aligned} \nabla \rho \cdot (x^2 z A, x z B, x z^2 C) \\ + \rho x z [2A + x \partial_x A + \partial_y B + 2C + z \partial_z C] = 0 \end{aligned}$$

or, equivalently,

$$\nabla \rho \cdot (x A, B, z C) + \rho [2A + x \partial_x A + \partial_y B + 2C + z \partial_z C] = 0 \quad (\text{A7})$$

By Eq. (A2), at the equilibrium \mathbf{p} , Eq. (A7) reduces to

$$2A(\mathbf{p}, 0) + \partial_y B(\mathbf{p}, 0) + 2C(\mathbf{p}, 0) = 0 \quad (\text{A8})$$

which is equivalent to Eq. (15) by Eq. (A4).

Acknowledgments

This work was supported by the U.S. Air Force Office of Scientific Research grant F49620-03-1-0200 and the National Science Foundation grant DMS-04-04845.

References

- [1] Prandtl, L., "Über Flüssigkeitsbewegung bei Sehr Kleiner Reibung," *Verhandlungen des 3 Internationalen Mathematiker-Kongresses*, Teubner, Leipzig, Germany, 1904, pp. 484–491.
- [2] Chapman, G. T., "Topological Classification of Flow Separation on Three-Dimensional Bodies," AIAA Paper 86-0485, 1986.
- [3] Détery, J. M., "Robert Legendre and Henri Werlé: Toward the Elucidation of Three-Dimensional Separation," *Annual Review of Fluid Mechanics* Vol. 33, 2001, pp. 129–54.
- [4] Peake, D. J., and Tobak, M., "Topological Structure of Three-Dimensional Separated Flows," AIAA Paper 81-1260, 1981.
- [5] Simpson, R. L., "Aspects of Turbulent Boundary Layer Separation," *Progress in Aerospace Sciences*, Vol. 32, Oct. 1996, pp. 457–521.
- [6] Tobak, M., and Peake, D. J., "Topology of Three-Dimensional Separated Flows," *Annual Review of Fluid Mechanics*, Vol. 14, 1982, pp. 61–85.
- [7] Legendre, R., "Séparation de l'Écoulement Laminaire Tridimensionnel," *Recherche Aéronautique*, Vol. 54, 1956, pp. 3–8.
- [8] Dallmann, U., "Topological Structures of Three-Dimensional Flow Separation," *DFVLR Nachrichten : Mitteilungsblatt der Deutschen Forschungs- und Versuchsanstalt für Luft- und Raumfahrt (DFVLR)*, Vol. 1B, 1983, pp. 221–282.
- [9] Hunt, J. C. R., Abell, C. J., Peterka, J. A., and Woo, H., "Kinematical Studies of the Flows Around Free or Surface Mounted Obstacle; Applying Topology to Flow Visualization," *Journal of Fluid Mechanics*, Vol. 86, 1978, pp. 179–200.
- [10] Perry, A. E., and Fairlie, B. D., "Critical Points in Flow Patterns," *Advances in Geophysics*, Vol. 18, Apr. 1974, pp. 200–215.
- [11] Yates, L. A., and Chapman, G. T., "Streamlines, Vorticity Lines, and Vortices Around Three-Dimensional Bodies," *AIAA Journal*, Vol. 30, No. 7, 1992, pp. 1819–1826.
- [12] Lighthill, M. J., "Attachment and Separation in Three-Dimensional Flows," *Laminar Bound. Layer Theory*, edited by L. Rosenhead, Oxford Univ. Press, New York, 1963, pp. 72–82.
- [13] Wang, K. C., "Separation Patterns of Boundary Layer over an Inclined Body of Revolution," *AIAA Journal*, Vol. 10, No. 8, 1972, 1044–1050.
- [14] Wu, J. Z., Gu, J. W., and Wu, J. M., "Steady Three-Dimensional Fluid Particle Separation from Arbitrary Smooth Surface and Formation of Free Vortex Layers," AIAA Paper 87-2348, 1987.
- [15] Van Dommelen, L. L., and Cowley, S. J., "On the Lagrangian Description of Unsteady Boundary Layer Separation, Part 1: General Theory," *Journal of Fluid Mechanics*, Vol. 210, Jan. 1990, pp. 593–626.

- [16] Wu, J. Z., Tramel, R. W., Zhu, F. L., and Yin, X. Y., "A Vorticity Dynamics Theory of Three-Dimensional Flow Separation," *Physics of Fluids, A/Fluid Dynamics*, Vol. 12, No. 8, Aug. 2000, pp. 1932–1954.
- [17] Williams, P. T., and Barker, A. J., "Numerical Simulations of Laminar Flow over a 3-D Backward-Facing Step," *International Journal for Numerical Methods in Fluids*, Vol. 24, No. 11, 1997, pp. 1159–1183.
- [18] Biswas, G., Breuer, M., and Durst, F., "Backward-Facing Step Flows for Various Expansion Ratios at Low and Moderate Reynolds Numbers," *Transactions of the ASME*, Vol. 126, May 2004, pp. 362–374.
- [19] Nie, J. H., and Armaly, B. F., "Reverse Flow Regions in Three-Dimensional Backward-Facing Step Flow," *International Journal of Heat and Mass Transfer*, Vol. 47, No. 22, 2004, pp. 4713–4720.
- [20] Nie, J. H., and Armaly, B. F., "Reattachment of Three-Dimensional Flow Adjacent to Backward-Facing Step," *Transactions of the ASME*, Vol. 125, No. 3, 2003, pp. 422–428.
- [21] Stüer, H., Gyr, A., and Kinzelbach, W., "Laminar Separation on a Forward Facing Step," *European Journal of Mechanics, B/Fluids*, Vol. 18, No. 4, 1999, pp. 675–692.
- [22] Wilhelm, D., Härtel, C., and Kleiser, L., "Computational Analysis of the Two-Dimensional-Three-Dimensional Transition in Forward-Facing Step Flow," *Journal of Fluid Mechanics*, Vol. 489, Aug. 2003, pp. 1–27.
- [23] Surana, A., Grunberg, O., and Haller, G., "Exact Theory of Three-Dimensional Flow Separation, Part 1: Steady Separation," *Journal of Fluid Mechanics*, Vol. 564, Sept. 2006, pp. 57–103.
- [24] Jacobs, G. B., Kopriva, D. A., and Mashayek, F., "Validation Study of a Multidomain Spectral Code for Simulation of Turbulent Flows," *AIAA Journal*, Vol. 43, No. 6, 2005, pp. 1256–1264.
- [25] Jacobs, G. B., Kopriva, D. A., and Mashayek, F., "A Conservative Isothermal Wall Boundary Condition for the Compressible Navier–Stokes Equations," *Journal of Scientific Computing*, Vol. 30, No. 2, 2007, pp. 177–192.
- [26] Gresho, P. M., Garting, D. K., Cliffe, K. A., Winters, K. H., Garratt, T. J., Spence, A., and Goodrich, J. H., "Is the Steady Viscous Incompressible Two-Dimensional Flow over a Backward-Facing Step at $Re = 800$ Stable?," *International Journal for Numerical Methods in Fluids*, Vol. 17, No. 6, Sept. 1993, pp. 501–541.
- [27] Armaly, B. F., Durst, F., Pereira, J. C. F., and Schonung, B., "Experimental and Theoretical Investigation of Backward-Facing Step Flow," *Journal of Fluid Mechanics*, Vol. 127, 1983, pp. 473–496.
- [28] Shankar, P. N., and Deshpande, M. D., "Fluid Mechanics in the Driven Cavity Flow," *Annual Review of Fluid Mechanics*, Vol. 32, 2000, pp. 93–136.
- [29] Ghis, U., Ghia, K. N., and Shin, C. T., "High- Re Solutions for Incompressible Flow Using the Navier–Stokes Equations and a Multigrid Method," *Journal of Computational Physics*, Vol. 48, Dec. 1982, pp. 387–411.
- [30] Wetzel, G. W., Simpson, R. L., and Chesnakas, C. J., "Measurement of Three-Dimensional Crossflow Separation," *AIAA Journal*, Vol. 36, No. 4, 1998, pp. 557–564.
- [31] Haller, G., Surana, A., and Jacobs, G. B., "Finding the Separation Line in Open Separation," *Physics of Fluids* (to be submitted for publication).
- [32] Surana, A., Jacobs, G. B., Grunberg, O., and Haller, G., "Exact Theory of Three-Dimensional Flow Separation, Part 2: Fixed Unsteady Separation," *Journal of Fluid Mechanics* (submitted for publication).
- [33] Haller, G., "Exact Theory of Unsteady Separation for Two-Dimensional Flows," *Journal of Fluid Mechanics*, Vol. 512, Aug. 2004, pp. 257–311.
- [34] Kilic, M. S., Haller, G., and Neishtadt, A., "Unsteady Fluid Flow Separation by the Method of Averaging," *Physics of Fluids*, Vol. 17, June 2005, pp. 67–104.

X. Zhong
Associate Editor